Quantum dot–quantum dot interactions mediated by a metal nanoparticle: Towards a fully quantum model

Ryan D. Artuso* and Garnett W. Bryant
Joint Quantum Institute and Quantum Measurement Division, National Institute of Standards and Technology, Gaithersburg, Maryland 20899-8423, USA
(Received 20 December 2012; published 21 March 2013)

We study the interactions between two semiconductor quantum dots (SQDs) coupled to a metal nanoparticle using different approximations. In particular, we identify and address issues in modeling the system using a semiclassical approach. We find that a semiclassical approach to model the coupling between the SQDs can lead to unstable, oscillatory, and chaotic behavior in a strong SQD–SQD coupling regime. This nonlinear behavior is shown to be due to a breaking of the identical particle symmetry. Additionally, we see that this chaotic behavior is closely related to the type of decoherence present in the system, specifically, whether the decoherence is collective or noncollective between the two SQDs. This provides insight into proper accounting of these important, but often neglected, interactions. When the system is modeled using a more quantum mechanical approach, this chaotic regime is absent. Finally, we compare the two models on a system with a strong plasmon-mediated interaction between the SQDs and a weak direct interaction between them. In this case, we find that while the results of the two models are similar, dipole blockade and the level splitting of the single-exciton states in the quantum model give rise to nontrivial differences between the two models.

DOI: 10.1103/PhysRevB.87.125423 PACS number(s): 78.67.Hc, 78.67.Bf, 78.20.Bh

I. INTRODUCTION

The nanoscale transmission of quantum information and excitations between qubits for quantum communication, quantum computing, and quantum measurement will require transfer where the quantum character of the information can be maintained. At submicron distances, this means directed transmission must be carried out with better than wavelength-scale resolution. One possible solution to this limitation is coupling qubits, for example in quantum dots, to plasmonic structures. It has been predicted that below the diffraction limit, highly efficient directed energy transfer over plasmonic wires consisting of chains of closely spaced metal nanoparticles could be achieved.[1] Furthermore, it has been predicted that large entanglement, either spontaneously formed or in a continuously driven steady state, would be possible between qubits coupled to a plasmonic waveguide over distances exceeding a wavelength.[2] Lastly, it is worth noting that by coupling the broad, continuous, plasmonic response of plasmons to the discrete excitons of quantum emitters, these structures are an ideal system to study at the interface between classical and quantum physics.

Several recent experiments have already shown very promising results in these structures. Efficient exciton-plasmon-photon conversion and an enhanced emission rate with the coupling of a CdSe quantum dot to a silver nanowire have been demonstrated.[3,4] When coupled to elongated metal nanoparticles, the photoluminescence intensity of quantum dots is enhanced in a polarization-selective way,[5] and when coupled with a nano-optical Yagi-Uda antenna, the quantum dot emission can be made unidirectional.[6] Exciting results have been attained showing that quantum coherence can survive in plasmonic structures, such as the transportation of entangled photons by surface plasmons[7] and the energy-time entanglement of a pair of photons following a photon-plasmon-photon conversion.[8] Furthermore, it has been demonstrated that during plasmon propagation in metallic waveguides, losses appear to follow a linear uncorrelated Markovian model of damping at the single quanta level, showing the quantum regime of plasmonics is realistic.[9] In related work, the quantum statistics of the light from a quantum emitter (in this case, the color center of a nanodiamond) was shown to be preserved after conversion to plasmons and propagation in a polycrystalline gold film.[10] Recently, researchers have shown that using a two-step lithographic process, with the first step resulting in a polymer template, it is possible to control the deposition of quantum dots near nanowires, which should make more complicated structures accessible in the near future.[11]

Previously, the modified, hybrid response of a single semiconductor quantum dot (SQD) coupled to a nearby metallic nanoparticle (MNP), using semiclassical approximations, has been extensively studied[12–19] in the weak coupling regime,[12] in a strong coupling regime,[13–16] and with multiple metal nanoparticles.[17,18] Also, it has been predicted that a single emitter coupled to the plasmonic cavity of a patch antenna can exhibit a large Purcell factor, collection efficiency, and spectral width.[20] Furthermore, a cross-shaped nanoantenna driven by a quantum dot has been proposed as a source of polarization entangled photons, offering both large enhancement to the spontaneous emission rate of the SQD and high extraction efficiency.[21]

Recently, several theoretical investigations have gone beyond the semiclassical limit in studying this system by treating the plasmon-exciton interaction with quantum mechanical methods, such as treating the plasmon in the quasimode formalism commonly employed in cavity QED.[22] When the semiclassical results of a single quantum dot interacting with a metal nanoparticle are compared to a cavity-QED treatment, the semiclassical results can be corrected by properly accounting for dephasing by using a random phase jump method.[23] Also, by using a Green's function approach to study a system comprised of one or two quantum emitters coupled through

a nanorod, an optimal emitter-wire separation for excitation-plasmon conversion was found and plasmon-mediated coupling between the two emitters was studied.[24] In addition to quantizing the local field produced by the metal particle, progress has been made in better understanding the inherent quantum properties of very small metal particles, including size quantization effects[25,26] and the plasmon coupling to atomic-scale transport.[27]

We discuss here the response of a hybrid nanostructure molecule consisting of two SQDs coupled to a single MNP, subject to an applied electric field. The field couples to both of the SQDs as well as the MNP, and all three constituents interact with each other through a dipole-dipole coupling. To model such a complex system, a number of approximation schemes must be employed. Different choices for the approximations can result in predictions that differ both qualitatively and quantitatively. Therefore, a careful examination is needed of the various techniques that are commonly employed.

Furthermore, with two SQDs being considered as part of an open quantum system, the nature of the coupling to the bath is of increased importance. Two identical quantum objects, coupled in phase to the *same* bath mode, will decohere collectively. However, a slight detuning of their resonances will introduce a decoherence in each object independent of the other (and thus noncollective). Coupling to bath modes *internal* to each object, respectively (exciton-phonon coupling inside a quantum dot, for example[28]), introduces an additional source of noncollective decoherence. This question of collective versus noncollective decoherence can determine if and how a symmetry can be broken, further complicating the modeling of the system.

The focus of this paper is to identify and address these issues in modeling hybrid systems. Using a semiclassical approach to model the coupling between the SQDs, we find that such an approximation can lead to unstable, oscillatory, and chaotic behavior in the strong SQD–SQD coupling regime. This nonlinear behavior is shown to be due to a breaking of the identical particle symmetry. When the system is modeled using a quantum mechanical model for the SQD–SQD coupling, this instability is removed. Additionally, we see that this chaotic behavior is closely related to the type of decoherence present in the system, specifically, whether the decoherence is collective or noncollective between the two SQDs. This provides insight into the proper accounting of these important, but often neglected, interactions.

The paper is organized as follows. In Sec. II, we look at the SQD–MNP–SQD molecule in detail and discuss various models to describe it. In Sec. III, we use a simple semiclassical approach to model the system and find a regime of highly chaotic behavior in the case of identical SQDs. We explore this behavior in detail and see that it is due to a symmetry breaking induced by noncollective decoherence. Additionally, we find that this chaotic behavior is removed from the system with an increased coupling to the MNP. The coupling to the classical plasmon of the MNP in this model effectively washes out the nonlinear effect. In Sec. IV, we replace the semiclassical SQD–SQD direct coupling term with a quantum mechanical interaction term consistent with molecular quantum electrodynamics. In this case, we note the absence of the chaotic behavior. In its place, we find a dipole blockade induced by the splitting of the symmetric and antisymmetric SQD eigenstates. We then take a closer look at dipole blockade and compare the two models in the weak SQD–SQD coupling regime. Finally, we present our conclusions in Sec. V.

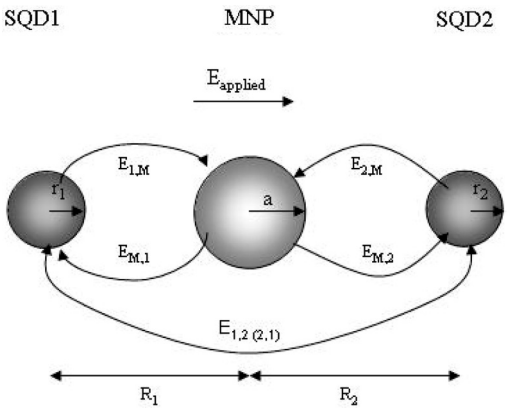

FIG. 1. An applied field induces a polarization in the MNP and both SQDs, which in turn allows for a dipole-dipole coupling between the three particles.

II. SQD–MNP–SQD HYBRID MOLECULE

We consider a hybrid nanomolecule composed of two SQDs with radii r_1 and r_2 interacting with a spherical MNP of radius a, separated from the MNP by the center-to-center distances R_1 and R_2, respectively (see Fig. 1). The entire system is subject to an applied electric field $E = E_0 \cos(\omega t)$, where E_0 is the magnitude of the driving field and ω is the angular frequency at which it oscillates. We model the SQDs as spherical semiconductors with a dipole located at the center of each. We treat the SQDs as an effective two-level quantum system in the density matrix formalism with exciton energies $\hbar\omega_1$ and $\hbar\omega_2$, transition dipole moments μ_1 and μ_2, and dielectric constants ϵ_1 and ϵ_2. In the dipole limit, only the three bright excitons (one for each optical axis) of each SQD participate in the interaction. The direction of the applied field determines which exciton is excited. However, dark excitons do contribute to the exciton lifetime. We treat the MNP as a classical spherical dielectric particle with dielectric function $\epsilon_M(\omega)$, and imagine the entire system to be embedded in a material of dielectric constant ϵ_B.

Each quantum dot has three interactions. The first is the direct coupling to the applied field. Second, each SQD interacts with the electric field produced by the MNP. Last, the SQDs interact with each other. Similarly, the MNP responds to the applied field as well as to each SQD. We solve the system self-consistently.

We begin by writing the Hamiltonian for the two SQDs $\mathcal{H}_{\text{total}}$ as

$$\mathcal{H}_{\text{total}} = \hbar\omega_1 \hat{a}_1^\dagger \hat{a}_1 + \hbar\omega_2 \hat{a}_2^\dagger \hat{a}_2 + \mathcal{H}_{1\leftrightarrow 2} - \mu_1 E_{\text{SQD1}} (\hat{a}_1 + \hat{a}_1^\dagger) - \mu_2 E_{\text{SQD2}} (\hat{a}_2 + \hat{a}_2^\dagger),$$

where $\hat{a}_{1(2)}$ and $\hat{a}_{1(2)}^\dagger$ are the exciton annihilation and creation operators for SQD1(2) and $\mathcal{H}_{1\leftrightarrow 2}$ represents the direct coupling between SQD1 and SQD2. E_{SQD1} is the electric field at the center of SQD1 that consists of the applied, external field E,

and the induced field produced by the polarization of the MNP $E_{M,1}$. Thus, E_{SQD1} is

$$E_{\mathrm{SQD1}} = \frac{1}{\epsilon_{\mathrm{eff1}}}(E + E_{M,1}), \tag{1}$$

where $\epsilon_{\mathrm{eff1}} = \frac{2\epsilon_{\mathrm{B}}+\epsilon_1}{3\epsilon_{\mathrm{B}}}$ is the screening factor of SQD1. The field on SQD1 from the MNP is

$$E_{M,1} = \frac{1}{4\pi\epsilon_{\mathrm{B}}}\frac{s_\alpha P_{\mathrm{MNP}}}{R_1^3}, \tag{2}$$

where $s_\alpha = 2$ (-1) when the applied field is parallel (perpendicular) to the major axis of the system. (E_{SQD2} is calculated similarly.)

In the dipole limit, the polarization of the MNP is[29]

$$P_{\mathrm{MNP}} = (4\pi\epsilon_{\mathrm{B}})\gamma a^3\left(E + \frac{1}{4\pi\epsilon_{\mathrm{B}}}\frac{s_\alpha P_{\mathrm{SQD1}}}{\epsilon_{\mathrm{eff1}}R_1^3} + \frac{1}{4\pi\epsilon_{\mathrm{B}}}\frac{s_\alpha P_{\mathrm{SQD2}}}{\epsilon_{\mathrm{eff2}}R_2^3}\right),$$

where $\gamma = \frac{\epsilon_M(\omega)-\epsilon_{\mathrm{B}}}{2\epsilon_{\mathrm{B}}+\epsilon_M(\omega)}$. Making use of the density matrix ρ to calculate the polarization of the SQD, we take the ensemble average of the dipole moment. We take as our states $|1\rangle = |00\rangle$, $|2\rangle = |10\rangle$, $|3\rangle = |01\rangle$, and $|4\rangle = |11\rangle$ (where, for example, $|10\rangle$ is the state with SQD1 excited and SQD2 in its ground state). We then have $P_{\mathrm{SQD1}} = \mu_1(\rho_{12} + \rho_{21} + \rho_{34} + \rho_{43})$ and $P_{\mathrm{SQD2}} = \mu_2(\rho_{13} + \rho_{31} + \rho_{24} + \rho_{42})$ (see Ref. 30). This allows us to write E_{SQD1}, but we still need an expression for $\mathcal{H}_{1\leftrightarrow 2}$ to complete our calculation of $\mathcal{H}_{\mathrm{total}}$.

A. SQD–SQD interaction

We have several choices for the SQD–SQD coupling terms in our Hamiltonian. If we treat the field produced by the SQD1 as a classical electric field produced by a dipole with polarization $P_{\mathrm{SQD1}} = \mu_1(\rho_{12} + \rho_{21} + \rho_{34} + \rho_{43})$ (similarly for SQD2), as we did in treating SQD–MNP interactions, then we have

$$\begin{aligned}\mathcal{H}_{1\leftrightarrow 2} &= -\mu_1\vec{\mathbf{E}}_{2\to 1}(\hat{a}_1 + \hat{a}_1^\dagger) - \mu_2\vec{\mathbf{E}}_{1\to 2}(\hat{a}_2 + \hat{a}_2^\dagger),\\ \mathcal{H}_{1\leftrightarrow 2} &= -\mu_1\frac{1}{4\pi\epsilon_{\mathrm{B}}}\frac{s_\alpha P_{\mathrm{SQD2}}}{\epsilon_{\mathrm{eff2}}\epsilon_{\mathrm{eff1}}(R_1+R_2)^3}(\hat{a}_1 + \hat{a}_1^\dagger)\\ &\quad - \mu_2\frac{1}{4\pi\epsilon_{\mathrm{B}}}\frac{s_\alpha P_{\mathrm{SQD1}}}{\epsilon_{\mathrm{eff1}}\epsilon_{\mathrm{eff2}}(R_1+R_2)^3}(\hat{a}_2 + \hat{a}_2^\dagger).\end{aligned}$$

In taking this approach, we are assuming that we can replace a quantized field, produced by the exciton, with a mean field value computed by the density matrix. This is a semiclassical approximation.

Alternatively, we can calculate this interaction with quantum electrodynamics. Two identical, two-level molecules interacting with a common electromagnetic mode, with a radiative decay rate $\gamma_{\mathrm{emitter}} = \frac{1}{\tau}$, separated by a distance d, have an interaction Hamiltonian of the form[31]

$$\mathcal{H}_{1\leftrightarrow 2} = \hbar\,\delta\,(\hat{a}_1 + \hat{a}_1^\dagger)\,(\hat{a}_2 + \hat{a}_2^\dagger), \tag{3}$$

where δ, the interaction energy, is calculated in the dipole limit as

$$\begin{aligned}\delta = \frac{3}{4\tau}\Bigg[&[\cos^2(\theta) - 1]\frac{\cos(\zeta)}{\zeta}\\ &+ [1 - 3\cos^2(\theta)]\left(\frac{\cos(\zeta)}{\zeta^3} + \frac{\sin(\zeta)}{\zeta^2}\right)\Bigg],\end{aligned} \tag{4}$$

where $\zeta = \frac{\omega d}{c}$, c is the speed of light, and θ denotes the phase difference of the bath mode at the locations of the two molecules.

B. Numerical calculations

We take E parallel to the axis of our SQD–MNP–SQD molecule (unless otherwise noted), i.e., $s_\alpha = 2$ and we take the dielectric constant of the background to be $\epsilon_B = \epsilon_0$. For the MNP, we take $\epsilon_M(\omega)$ as the bulk dielectric constant of gold as found experimentally.[32] For a small, spherical, gold MNP, the response has a broad plasmon peak near 2.4 eV with a width of approximately 0.25 eV. We let the radius of the MNP vary between 3 and 8 nm.

For the SQDs, we take $\epsilon_1 = \epsilon_2 = 6\,\epsilon_0$ and for the exciton resonant frequency we take it to be 2.5 eV, which is near the broad plasmon frequency of gold. For the MNP size regime we consider, the plasmon resonance for a sphere varies little with particle size. However, the size, shape, and material of the SQD strongly determine both the exciton energy level and its dipole moment. In this paper, we consider the simplest model and ignore this size dependence. While this is an oversimplification, it allows us to identify the range of optical signatures which are possible in the strong-field limit. Recent measurements of SQD dipole moments have yielded values of ≈ 1 e nm for self-assembled QDs (Ref. 33) and several times that for interface fluctuation QDs.[34] For the dipole moments of the SQDs, we let them vary between 0.25 and 4.0 e nm, corresponding to a SQD size of 2 to 20 nm. For the purposes of this investigation, this range is a reasonable coverage of the observed values that allows us to test the full spectrum of behavior.

III. SEMICLASSICAL APPROACH TO SQD–SQD COUPLING

We first model the system using the semiclassical approximation for the SQD–SQD coupling. Our Hamiltonian becomes

$$\begin{aligned}\mathcal{H}_{\mathrm{total}} = &\hbar\omega_1\hat{a}_1^\dagger\hat{a}_1 + \hbar\omega_2\hat{a}_2^\dagger\hat{a}_2\\ &- 2\hbar\cos\omega t\,\Omega_1\,(\hat{a}_1 + \hat{a}_1^\dagger) - 2\hbar\cos\omega t\,\Omega_2\,(\hat{a}_2 + \hat{a}_2^\dagger)\\ &- \hbar G_1(\rho_{12} + \rho_{21} + \rho_{34} + \rho_{43})\,(\hat{a}_1 + \hat{a}_1^\dagger)\\ &- \hbar G_2(\rho_{13} + \rho_{31} + \rho_{24} + \rho_{42})\,(\hat{a}_2 + \hat{a}_2^\dagger)\\ &- \hbar F(\rho_{12} + \rho_{21} + \rho_{34} + \rho_{43})\,(\hat{a}_2 + \hat{a}_2^\dagger)\\ &- \hbar F(\rho_{13} + \rho_{31} + \rho_{24} + \rho_{42})\,(\hat{a}_1 + \hat{a}_1^\dagger),\end{aligned}$$

where we have defined

$$G_1 = \frac{\gamma a^3 \mu_1^2 s_\alpha^2}{4\pi\epsilon_B \epsilon_{\text{eff1}} \hbar R_1^6},$$
$$\Omega_1 = \frac{E_0 \mu_1}{2\hbar}\left(1 + \frac{\gamma a^3 s_\alpha}{\epsilon_{\text{effM}} R_1^3}\right),$$
$$F = \frac{\mu_1 \mu_2 s_\alpha^2}{4\pi\epsilon_B \epsilon_{\text{eff1}} \epsilon_{\text{eff2}} \hbar}\left(\frac{1}{(R_1+R_2)^3} + \frac{\gamma a^3}{R_1^3 R_2^3}\right),$$

G_2 and Ω_2 are defined similarly. G_1 arises when the applied field polarizes SQD1, which in turn polarizes the MNP and then produces a field to interact back on SQD1. Thus, this can be thought of as the self-interaction of SQD1 because this coupling to SQD1 depends on the polarization of SQD1. The first term in Ω_1 is just the direct coupling to the applied field and the second term is the field from the MNP that is induced by the applied field. F arises from the interaction between the two dots. The first term is the direct coupling and the second term is the interaction mediated by the MNP.

We solve the master equation

$$\dot{\rho} = \frac{i}{\hbar}[\rho, \mathcal{H}_{\text{SQD}}] - \Gamma(\rho), \tag{5}$$

where $\Gamma(\rho)$ is the relaxation matrix. To find the entries of $\Gamma(\rho)$, we assume the baths of our SQDs are uncorrelated. For a noninteracting system, we could write $\rho = \rho^{(2)} \otimes \rho^{(1)}$ where $\rho^{(1)}$ and $\rho^{(2)}$ are the 2×2 density matrix in the single SQD case for SQD1 and SQD2, respectively, and ρ is the 4×4 density matrix for the combined system. We use this relation and the relaxation matrix for a single SQD with entries $\Gamma_{11}^{(1)} = \frac{\rho_{11}^{(1)}-1}{\tau_1}$, $\Gamma_{12}^{(1)} = \Gamma_{21}^{(1)*} = \frac{\rho_{12}^{(1)}}{T_1}$, and $\Gamma_{22}^{(1)} = \frac{\rho_{22}^{(1)}}{\tau_1}$ where the superscript indicates this is for SQD1 (similarly for SQD2). Making use of the master equation and $\rho = \rho^{(2)} \otimes \rho^{(1)}$, we arrive at the 4×4 matrix $\Gamma(\rho)$ for a noninteracting 2 SQD system:

$$\Gamma(\rho) = \begin{pmatrix} -\frac{\rho_{22}}{\tau_1} - \frac{\rho_{33}}{\tau_2} & \frac{\rho_{12}}{T_1} - \frac{\rho_{34}}{\tau_2} & \frac{\rho_{13}}{T_2} - \frac{\rho_{24}}{\tau_1} & \frac{\rho_{14}}{T_1} + \frac{\rho_{14}}{T_2} \\ \frac{\rho_{21}}{T_1} - \frac{\rho_{43}}{\tau_2} & \frac{\rho_{22}}{\tau_1} - \frac{\rho_{44}}{\tau_2} & \frac{\rho_{23}}{T_1} + \frac{\rho_{23}}{T_2} & \frac{\rho_{24}}{T_2} + \frac{\rho_{24}}{\tau_1} \\ \frac{\rho_{31}}{T_2} - \frac{\rho_{42}}{\tau_1} & \frac{\rho_{32}}{T_1} + \frac{\rho_{32}}{T_2} & \frac{\rho_{33}}{\tau_2} - \frac{\rho_{44}}{\tau_1} & \frac{\rho_{34}}{T_1} + \frac{\rho_{34}}{\tau_2} \\ \frac{\rho_{41}}{T_1} + \frac{\rho_{41}}{T_2} & \frac{\rho_{42}}{T_2} + \frac{\rho_{42}}{\tau_1} & \frac{\rho_{43}}{T_1} + \frac{\rho_{43}}{\tau_2} & \frac{\rho_{44}}{\tau_1} + \frac{\rho_{44}}{\tau_2} \end{pmatrix}.$$

We assume that the same $\Gamma(\rho)$ applies if the two dots interact and ρ is no longer separable.

Again, from looking at the single dot case, we make the following factorizations analogous to those made in the SQD–MNP system:[13]

$$\begin{aligned} \rho_{12} &= (A_{12} + iB_{12})e^{i\omega t}, & \rho_{13} &= (A_{13} + iB_{13})e^{i\omega t}, \\ \rho_{14} &= (A_{14} + iB_{14})e^{2i\omega t}, & \rho_{23} &= (A_{23} + iB_{23}), \\ \rho_{24} &= (A_{24} + iB_{24})e^{i\omega t}, & \rho_{34} &= (A_{34} + iB_{34})e^{i\omega t}, \end{aligned} \tag{6}$$

and note that $\rho_{ij} = \rho_{ji}^*$. Making use of these definitions and the rotating-wave approximation, we arrive at a set of 16 coupled, nonlinear differential equations. For the SQD relaxation times in this model, we take $\tau_1 = \tau_2 = 0.8$ ns and $T_1 = T_2 = 0.3$ ns.

In the steady-state limit, we set the time derivative of the A's, B's, as well as the diagonal density matrix elements to zero. Due to the nonlinear nature of the differential equations, more than one steady-state solution can exist for certain values of the parameters. In these regions, we must solve the full set of dynamical equations, allowing them to evolve from the initial conditions for times on the order of 10 ns to reach the steady state.

A. Weak-field limit

In Fig. 2, we compare the response of the SQD–MNP–SQD system to that of the SQD–MNP system in the weak-field limit (intensity of 1 W/cm^2). For each system, we plot the absorption of the SQD(s) Q_{SQD}, the absorption of the MNP Q_{MNP}, and the absorption of the total system Q_{total}. In all the plots, we see that the peak of the response shifts and broadens for small values of particle separation. The shift and broadening of this resonance peak when the particles are very close shows a hybrid excitation with a shortened lifetime.

When we compare the response of the SQD–MNP–SQD system (top of Fig. 2) to that of the response of single SQD coupled to a spherical MNP (bottom of Fig. 2), we find an

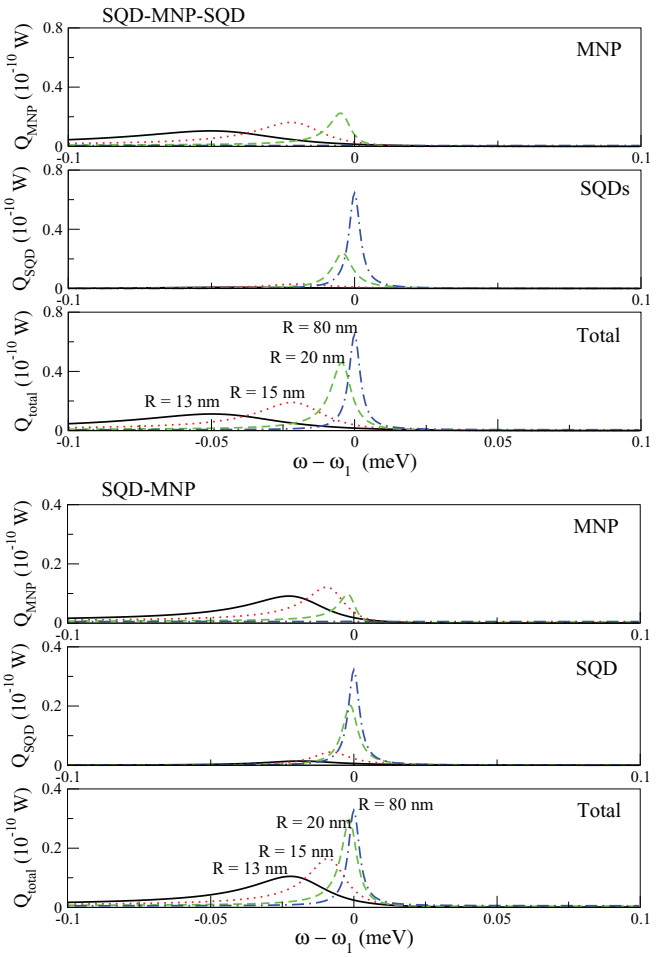

FIG. 2. (Color online) Energy absorption due to the MNP, the SQD, and the total, respectively, as a function of detuning, for two SQDs coupled to a spherical MNP (top), and for a single SQD coupled to a spherical MNP (bottom). All calculations were in the weak-field limit and particle separation was varied (the two SQD cases were treated symmetrically, $R = R_1 = R_2$, $\mu = \mu_1 = \mu_2$, and $\omega_1 = \omega_2 = 2.5$ eV). In both sets of plots, we take $a = 7.5$ nm and $\mu = 0.5$ e nm.

overall enhancement of the interaction. We first note that the magnitude of the absorption is nearly doubled when compared to the single SQD case for most particle separations. When the particles are far apart, the interparticle coupling is weak, and most of the absorption is due to the SQDs. Thus, the doubling is simply the absorption of the additional SQD. When the particles are close together, the interparticle coupling is strong and most of the absorption is in the MNP. The peak of the absorption in this case is due to the constructive interference of fields at the MNP, from the SQDs. Thus, the additional SQD doubles the magnitude of this field.

In addition to enhancing the magnitude of the absorption, we also have an increase in the interparticle coupling strength. This is evident in the increased shifting and slight broadening of the response, for a given R, when compared to the single SQD case. This indicates that a larger particle separation in the SQD–MNP–SQD system than in an SQD–MNP molecule can achieve a similar shift and broadening in the hybrid response.

B. Strong-field limit: a versus μ parameter space

We now consider the large-field limit as previously defined[12] (intensity of 10^3 W/cm^2). By manipulating a and μ ($\mu \equiv \mu_1 = \mu_2$), which are effectively the sizes of the MNP and SQDs, respectively, we can change the relative strengths of the local fields and, in turn, the strengths of the five different couplings (G, and the two terms that make up each of Ω and F). Looking at the solutions to the differential equations, both dynamically and in the steady-state limit, we find five distinct regimes of behavior in the a versus μ parameter space for a double SQD molecule (see the top of Fig. 3). Regions I, II, and III as well as the suppression regime were discussed in detail for an SQD–MNP molecule.[13,14] We direct the reader there for a full description of these effects. The new regime of behavior will be discussed in the following.

Comparing the parameter-space diagram of the SQD–MNP–SQD molecule to that of the SQD–MNP molecule (bottom of Fig. 3), we note several differences. First, we see that the threshold separating regions I and II is at a value of μ which is about half of that in the single SQD case. The appearance of an exciton-induced transparency (EXIT) occurs when the induced electric fields from the SQD overtake the applied field in magnitude at the location of the MNP. However, the addition of the second SQD effectively doubles the size of this internal field, which could equivalently be produced by an SQD with twice as large of a dipole moment. There is a similar effect that shifts the boundary between regions II and III, as well as the emergence of suppression. The appearance of bistability in the system is caused by feedback through the self-interaction. With the addition of a second SQD, there is increased feedback through the SQD–SQD interaction which leads to an enlargement in region III. This SQD–SQD interaction also provides the feedback for the constructive and destructive interference that leads to suppression. We see that not only does this enhance these effects, but it will also allow for the appearance of suppression even without the MNP, which obviously can not occur in the single SQD case. For an SQD–SQD molecule, the self-interaction is mediated by the coupling to the other SQD.

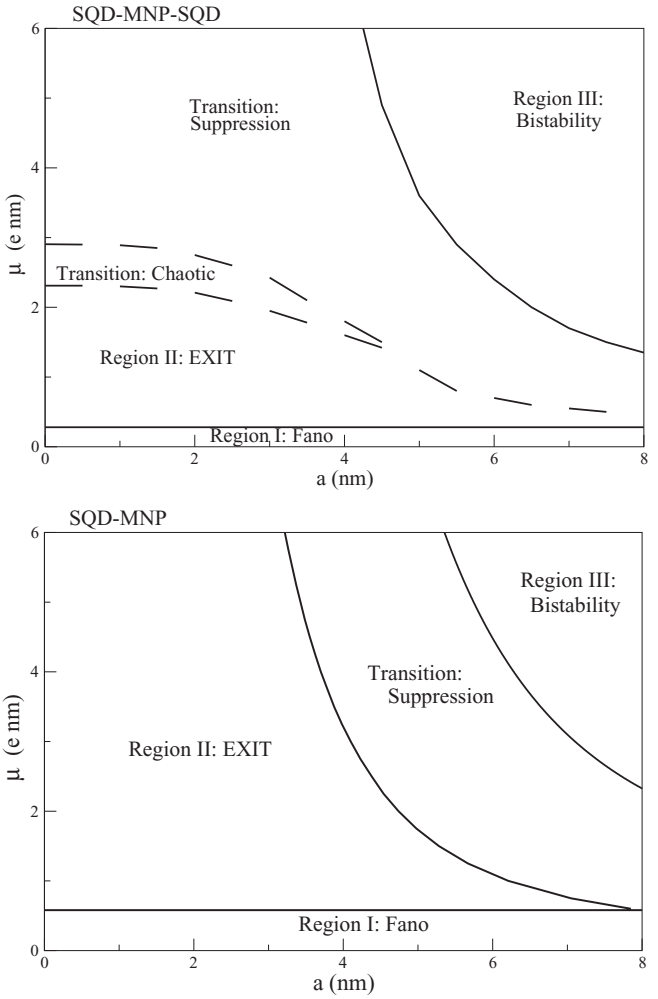

FIG. 3. μ vs a phase diagram comparison for $R = 13$ nm in the strong-field limit comparison between (bottom) an SQD–MNP system showing four regimes of behavior and (top) an SQD–MNP–SQD system showing five regimes of hybrid behavior.

C. Transition: Chaotic solutions

In addition to the enhancement in the appearance of EXIT, suppression, and bistability, we also note that the transition region is more complicated than in the single SQD case: chaotic behavior emerges from a strong SQD–SQD interaction. In fact, strong coupling to the MNP provides a quenching for this effect. Subsequently, it is best studied in the limit where there is no MNP ($a = 0$).

In this transition regime, for a range of frequencies just above the natural resonance of the SQDs, the system no longer reaches a steady state (see Fig. 4). In this frequency range ($\omega - \omega_0 \approx 35$ μeV to 50 μeV, with $\omega_0 \equiv \omega_1 = \omega_2$, for $a = 0$ nm, $\mu_1 = \mu_2 = 3.0$ e nm, and $R_1 = R_2 = 13$ nm), the solutions oscillate within a narrow envelope. We also note that despite the symmetry between the two SQDs, the population densities for the singly excited SQD states ρ_{22} and ρ_{33} are no longer identical for these solutions. We thus speculate that noise in the numerical calculations causes the symmetry to be broken. In fact, when the calculations are performed with increasingly greater numerical precision, much of this chaotic behavior can be eliminated. However, in our calculations, it

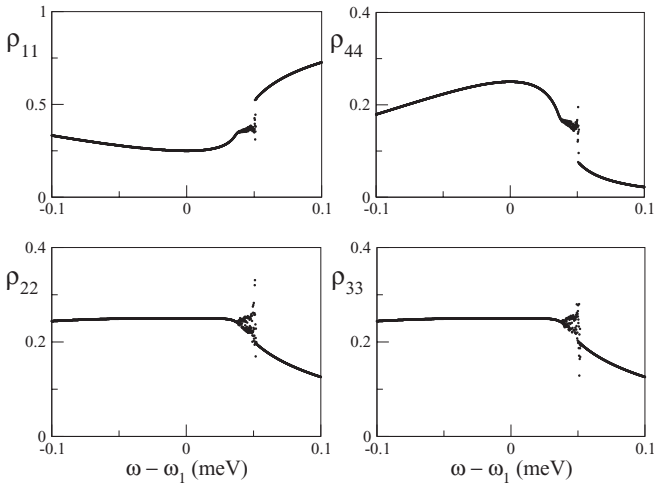

FIG. 4. Density matrix elements plotted as a function of detuning for two interacting, strongly coupled SQDs ($a = 0$ nm, $\mu_1 = \mu_2 =$ 3.0 e nm, and $R_1 = R_2 = 13$ nm). The response of the system shows discontinuity for detunings near 0.05 meV. For these frequencies, the system no longer reaches a steady state.

could never be removed completely, even when the numerical noise present in the system (less than 1 part in 10^{10}) was much smaller than the natural noise a realistic system would exhibit by at least several orders of magnitude.

1. *Explicit symmetry breaking*

To explore the effect of the SQD–SQD identical particle symmetry, we look at the effect of breaking it explicitly. This can best be done again without the presence of the MNP, and by slightly shifting the dipole moment, or the bare resonance frequency of one of the SQDs. However, care must be taken in detuning the SQD resonances as too large of a shift would cause them to uncouple.

When the SQD–SQD symmetry is broken explicitly, we see more chaotic behavior. We can see that the frequency range over which the system displays this oscillatory behavior increases (see Fig. 5 and the top left plot of Fig. 4 for comparison). As we noted above, when only numerical rounding provides the symmetry breaking, the range of frequencies over which the system oscillates is only 15 μeV. However, when the symmetry is broken explicitly, by either shifting one of the bare SQD resonances or by increasing one of the SQD dipole moments, this frequency range increases to around 125 μeV, nearly a full order of magnitude increase. This increase occurs even when the symmetry is broken by a trivial amount (1 part in 10^8) and increasing the numerical accuracy of the calculations no longer has any effect in reducing the chaotic behavior.

We also note that varying the amount by which the symmetry is broken is largely unimportant. Once a certain threshold is reached, the frequency range of the oscillations reaches a maximum, as does the envelope in which the solutions oscillate in. We do note, however, there is a small difference from the behavior shown in Fig. 4 and that in Fig. 5, which can be seen in the two rightmost plots in Fig. 5. The chaotic oscillations start from the edges of a frequency window with the innermost points displaying a more regular oscillatory nature.

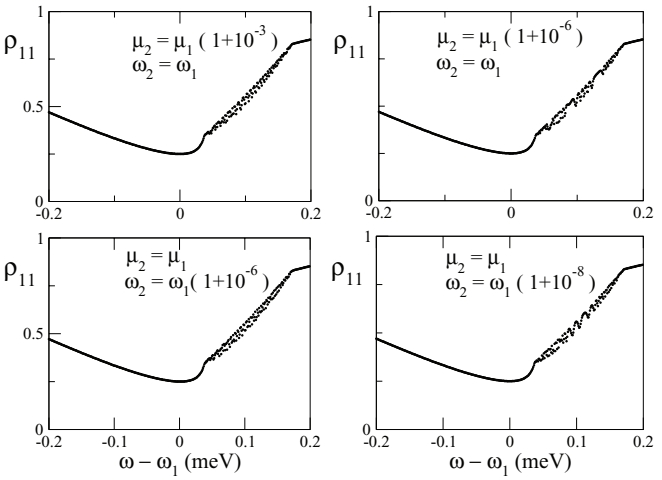

FIG. 5. ρ_{11} plotted as a function of the detuning between the driving field and SQD1 for four cases of explicit symmetry breaking. In all cases, $a = 0$ nm, $\mu_1 = 3.0$ e nm, and $R_1 = R_2 = 13$ nm were held fixed. The top two plots show $\mu_2 = \mu_1 + \delta$ symmetry breaking with $\omega_1 = \omega_2$. The bottom two plots show $\omega_2 = \omega_1 + \delta$ symmetry breaking with $\mu_1 = \mu_2$.

When we focus on a particular value of detuning inside the frequency window of this chaotic behavior, we see that the time evolution for that particular frequency is complicated, but more structured than scanning over the detuning would lead one to believe (Fig. 5). In Fig. 6, we see that the system initially undergoes fast oscillations due to Rabi flopping and the slight detuning ($t = 0$ ns to $\approx$1 ns). The system then settles into what would be a typical steady-state solution. Then, at a point between 2 and 5 ns, the system again acts as though it is far from equilibrium and undergoes large oscillations. Within a further 2 ns, the system then settles into a stable and undamped

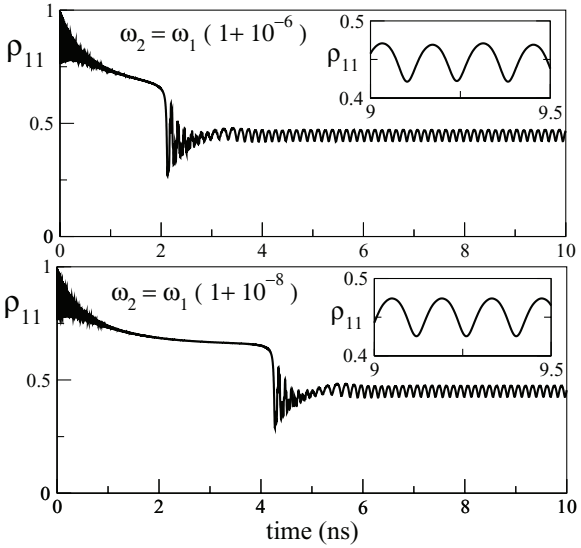

FIG. 6. Evolution of ρ_{11} as a function of time, for $a = 0$ nm, $\mu_1 = \mu_2 = 3.0$ e nm, $R_1 = R_2 = 13$ nm, and $\omega_1 = 2.5$ eV, for a driving frequency in the chaotic regime ($\omega - \omega_1 = 0.75$ meV). Shown are the responses for explicit symmetry breakings of ω_2 as labeled. Insets show that the frequency of the secondary oscillation does not appear to depend on the amount of the symmetry breaking.

oscillatory behavior. So, although the behavior appears to be very noisy when viewed as a function of driving frequency, for each particular frequency the behavior is very different than that of the weak-coupling regime, but still is predictable.

Furthermore, the frequency of these secondary oscillations appears to be unaffected by the degree of the symmetry breaking (see insets of Fig. 6). From the time evolution of ρ_{11}, we see that the secondary oscillations for an explicit symmetry breaking on the orders of 10^{-6} and 10^{-8} have nearly the same frequency. However, the onset into the oscillatory behavior can be significantly different, even for these small symmetry-breaking terms, with oscillatory behavior onset earlier in the case of the larger symmetry breaking (2 ns compared to 4 ns). This remains the case even for increasingly large symmetry breaking.

2. *Symmetric-antisymmetric basis*

We now focus on the behavior of the two individual SQDs when in this chaotic regime by looking at the probabilities that exactly one SQD is excited (ρ_{22} and ρ_{33}, respectively). In the absence of the MNP, with $\mu_1 = \mu_2 = 3.0$ e nm, $R_1 = R_2 = 13$ nm, $\omega_1 = 2.5$ eV, and $\omega_2 = \omega_1(1 + 10^{-8})$, and for a driving frequency in the chaotic regime ($\omega - \omega_1 = 0.75$ meV), we see that the two SQDs beat out of phase for times $t \geqslant 3$ ns (see Fig 7).

Due to the approximate symmetry between the dots, it is worthwhile to consider the symmetric and antisymmetric bases. We define the symmetric and antisymmetric states as

$$|\mathrm{S}\rangle = \frac{1}{\sqrt{2}}(|2\rangle + |3\rangle), \quad |\mathrm{A}\rangle = \frac{1}{\sqrt{2}}(|2\rangle - |3\rangle).$$

With these definitions, we can calculate the density matrix components for these new basis states as

$$\rho_{\mathrm{SS}} = \tfrac{1}{2}(\rho_{22} + \rho_{33} + \rho_{23} + \rho_{32}),$$
$$\rho_{\mathrm{AA}} = \tfrac{1}{2}(\rho_{22} + \rho_{33} - \rho_{23} - \rho_{32}).$$

When the SQD1–SQD2 symmetry is unbroken, $|\mathrm{S}\rangle$ is coupled to the driving field, while $|\mathrm{A}\rangle$ remains uncoupled. However, there is coupling to the antisymmetric state by means of relaxation matrix $\Gamma(\rho)$ due to the fact that we have thus far treated the SQDs' relaxation in a noncollective manner. For example, the double-exciton state $|4\rangle$ relaxes into both the symmetric state and antisymmetric state with equal probabilities. This can be seen in the right-hand side of Fig. 7. The symmetric state initially oscillates as the applied field drives the system, whereas the antisymmetric state slowly fills due to relaxation of $|4\rangle$, on a time scale corresponding to $\tau_1 = \tau_2 = 0.8$ ns.

In Fig. 7, we see that, initially, the system oscillates until damping causes it to begin to settle into a semistable steady state. At about $t = 1$ ns, the initial Rabi oscillations have damped out, ρ_{22} is nearly equal to ρ_{33}, and ρ_{SS} is nearly equal to ρ_{AA}. As the system continues to evolve, ρ_{33} begins to decrease, while ρ_{22} continues to climb. Meanwhile, both ρ_{AA} and ρ_{SS} slowly increase. This eventually culminates in the oscillations occurring at $t \approx 2$ ns. These oscillations eventually become regular as the system oscillates between two different steady states indefinitely. Returning to the a versus μ parameter space (top of Fig. 3), we see that the introduction of a small MNP ($a = 4$ nm) to mediate the interaction is enough to quench the SQDs from beating.

When the degree of symmetry breaking is held fixed, and the system evolution is analyzed for particular values of the detuning inside the frequency range of chaotic behavior, we see that the onset of the oscillations occurs sooner for frequencies near the endpoints of this window (see Fig. 8). For a fixed set of μ_1, μ_2, R_1, R_2, ω_1, and ω_2, the delay reaches a maximum of 4.5 ns at approximately $\omega - \omega_1 = 80$ μeV. We also note that near this maximum delay, the magnitude of the oscillations is greatest.

The maximum delay in the onset occurs at longer times for smaller symmetry-breaking terms (see Fig. 9). With $\mu_1 = 3.3$ e nm and $\mu_2 = \mu_1(1 + 10^{-10})$, the onset can take up to 40 ns for particular values of the detuning. In fact, with $\mu_2 = \mu_1(1 + 10^{-n})$, the peak in the onset appears to increase linearly with the exponent n [or equivalently $-\ln(\mu_2 - \mu_1)$]

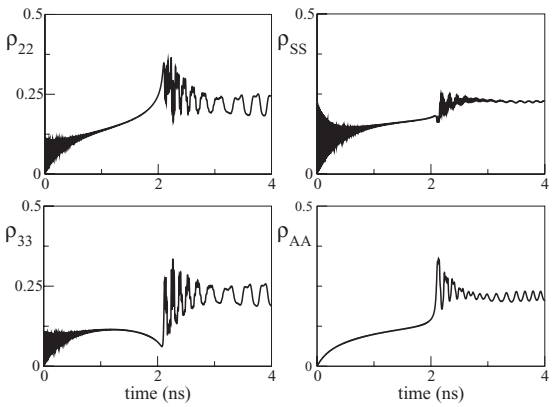

FIG. 7. Time evolution of ρ_{22}, ρ_{33}, ρ_{SS}, and ρ_{AA}, for $a = 0$ nm, $\mu_1 = \mu_2 = 3.0$ e nm, $R_1 = R_2 = 13$ nm, $\omega_1 = 2.5$ eV, and $\omega_2 = \omega_1(1 + 10^{-6})$, for a driving frequency in the chaotic regime ($\omega - \omega_1 = 0.75$ meV). ρ_{22}, ρ_{33}, and ρ_{SS} are initially driven and quickly oscillate, while ρ_{AA} slowly fills due to relaxation.

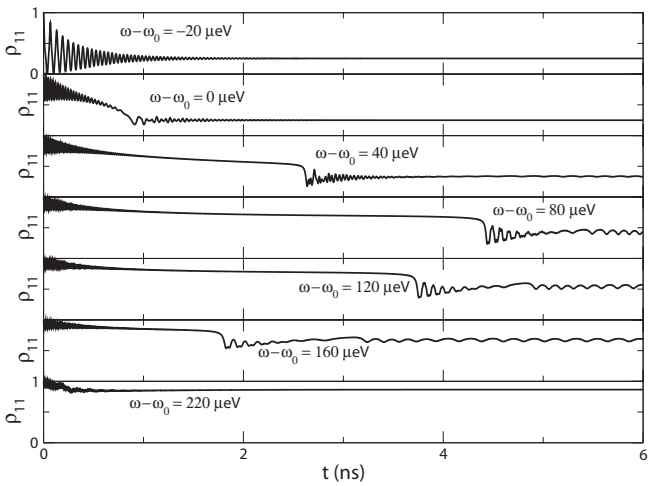

FIG. 8. The secondary oscillations occur over a range of the applied frequencies ($\omega - \omega_1 = 0$ μeV to 200 μeV). In all cases, the other system parameters and initial conditions are held fixed ($\mu_1 = 3.25$ e nm, $\mu_2 = 3.27$ e nm, $R_1 = R_2 = 13$ nm, $\omega_0 \equiv \omega_1 = \omega_2 = 2.5$ eV).

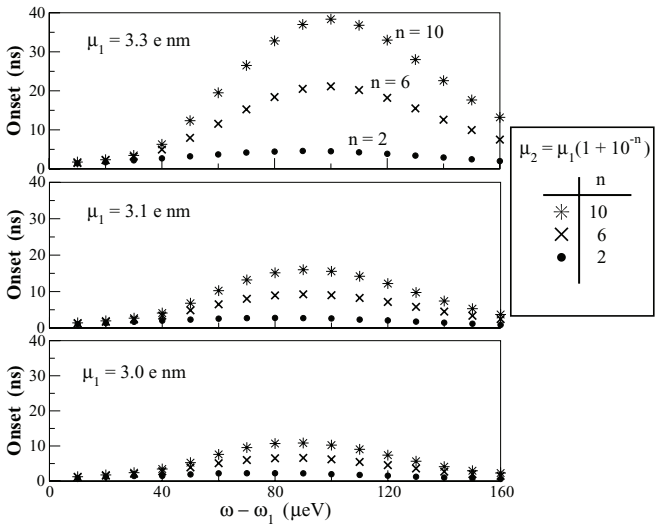

FIG. 9. The onset of chaotic behavior as a function of detuning for three regimes of symmetry breaking $\mu_2 = \mu_1(1 + 10^{-n})$ with $n = \{2,6,10\}$, plotted for each value of μ_1 as indicated. For each of the three plots we see that the delay in the onset increases as the magnitude of the symmetry breaking decreases. When the three plots are compared, the peak in the onset appears to shift to a larger detuning (from $\omega - \omega_1 = 90$ μeV to $\omega - \omega_1 = 100$ μeV) as the magnitude of μ_1 (and thus μ_2) increases from 3.0 to 3.3 e nm.

inside the chaotic regime. Over this range of n shown in the figure $[n = (2,10)]$, which covers eight orders of magnitude in the symmetry-breaking term, this relationship is found to be (including additional intermediate data points not shown in Fig. 9 for clarity)

$$t_{\text{onset}}^{(\max)} = \begin{cases} 1.08n + 0.11 & \text{for} \quad \mu_1 = 3.0\,\text{e nm}, \\ 1.66n - 0.62 & \text{for} \quad \mu_1 = 3.1\,\text{e nm}, \\ 4.23n - 4.15 & \text{for} \quad \mu_1 = 3.3\,\text{e nm}. \end{cases}$$

So, not only does onset increase linearly with increasing n, but it also increases with increased coupling strength (larger magnitude of μ_1, and thus μ_2). In addition to the increase in onset as the coupling strength increases, we also see that the detuning at which the peak in the onset occurs shifts to higher energies for a fixed value of n. For example, with $n = 10$, the detuning where the peak is located shifts from $\omega - \omega_1 = 90$ μeV to $\omega - \omega_1 = 100$ μeV, when μ_1 is increased from 3.0 to 3.3 e nm.

This relationship between the degree of symmetry breaking and the delay in onset explains what we saw in Fig. 5. There, we noticed that the plots on the right-hand side had a more regular behavior towards the middle of the frequency band that displays the chaotic behavior. However, in Fig. 9, we see that detunings near these frequencies take much longer for the onset of chaotic behavior. In these cases, the initial semistable state that the system first evolves into is more stable than for fields driving the system near the edges of the chaotic regime frequency window. Thus, a larger asymmetry must be built up in the system before the system can be knocked out of this semistable state, which accounts for this additional time.

Since the antisymmetric state is a higher-energy state than the symmetric state, the location of the antisymmetric resonance is above the bare resonance and is in fact in this chaotic region. Since the interaction term between the two SQDs is $\hbar F$, times the transition dipole moment operator, we can estimate the splitting between the symmetric and antisymmetric states to be $2\hbar F\,\langle\mu\rangle$. For $\mu_1 = 3.25$ e nm, $\mu_2 = 3.27$ e nm, $R_1 = R_2 = 13$ nm, this splitting is approximately 100 μeV, so we expect the antisymmetric mode to be around $\omega - \omega_1 = 50$ μeV which is very close to the location of the maximum delay in the onset of secondary oscillations. However, energy splitting and level repulsion between quantum levels is obviously a quantum effect, thus we can expect that the semiclassical approximation for the SQD–SQD coupling breaks down here.

IV. TOWARDS A MORE QUANTUM MECHANICAL APPROACH

Previously, we took the single SQD relaxation matrix as a basis to construct the two-particle relaxation matrix in order to model the interaction with the bath. If we define the Lindblad operator as

$$\mathcal{L}(\hat{A},\hat{B}) \equiv \hat{A}\rho\hat{B}^\dagger - \tfrac{1}{2}(\hat{B}^\dagger\hat{A}\rho + \rho\hat{B}^\dagger\hat{A}), \tag{7}$$

then this method is equivalent to taking four Lindblad terms, namely, relaxation of SQD1, $\mathcal{L}(\hat{a}_1,\hat{a}_1)$, relaxation of SQD2, $\mathcal{L}(\hat{a}_2,\hat{a}_2)$, dephasing of SQD1, $\mathcal{L}(\hat{a}_1^\dagger\hat{a}_1,\hat{a}_1^\dagger\hat{a}_1)$, and dephasing of SQD2, $\mathcal{L}(\hat{a}_2^\dagger\hat{a}_2,\hat{a}_2^\dagger\hat{a}_2)$. However, since we are treating the SQDs to be very close spatially, and very near to each other in resonance, they can both interact with the same bath. For example, both dots would interact with the same photon modes. As a consequence, spontaneous decay into these modes should occur due to the coherent response of the two dots (superradiance). Thus, there are two other Lindblad terms that we should consider, $\mathcal{L}(\hat{a}_1,\hat{a}_2)$ and $\mathcal{L}(\hat{a}_2,\hat{a}_1)$, i.e., a bath-induced interaction between the two dots. If we allow the two SQDs to interact with the same bath mode, then this should also be reflected in our Hamiltonian.

A. Quantum mechanical SQD–SQD coupling

We now instead use the quantum mechanical expression for the coupling between the two dots.[31] Our Hamiltonian is then

$$\begin{aligned} \mathcal{H}_{\text{total}} = {} & \hbar\omega_1\hat{a}_1^\dagger\hat{a}_1 + \hbar\omega_2\hat{a}_2^\dagger\hat{a}_2 \\ & - 2\hbar\cos\omega t\,\Omega_1\,(\hat{a}_1 + \hat{a}_1^\dagger) - 2\hbar\cos\omega t\,\Omega_2\,(\hat{a}_2 + \hat{a}_2^\dagger) \\ & - \hbar G_1(\rho_{12} + \rho_{21} + \rho_{34} + \rho_{43})\,(\hat{a}_1 + \hat{a}_1^\dagger) \\ & - \hbar G_2(\rho_{13} + \rho_{31} + \rho_{24} + \rho_{42})\,(\hat{a}_2 + \hat{a}_2^\dagger) \\ & - \hbar F_{\text{QM}}(\rho_{12} + \rho_{21} + \rho_{34} + \rho_{43})\,(\hat{a}_2 + \hat{a}_2^\dagger) \\ & - \hbar F_{\text{QM}}(\rho_{13} + \rho_{31} + \rho_{24} + \rho_{42})\,(\hat{a}_1 + \hat{a}_1^\dagger) \\ & + \hbar\delta(\hat{a}_1^\dagger\hat{a}_2 + \hat{a}_2^\dagger\hat{a}_1), \end{aligned}$$

where G and Ω terms are defined as before and F_{QM} is defined as

$$F_{\text{QM}} = \frac{\gamma a^3\mu_1\mu_2 s_\alpha^2}{4\pi\epsilon_{\text{B}}\epsilon_{\text{eff1}}\epsilon_{\text{eff2}}\hbar R_1^3 R_2^3}\,. \tag{8}$$

δ is as previously defined in Eq. (4). We still use the semiclassical expression for the MNP mediated coupling

between the dots (F_{QM}), but replace the direct coupling term with a quantum mechanical form.

To find the relaxation of the system, we now take a more complicated interaction Hamiltonian with the reservoir $\mathcal{H}_{\mathcal{R}}$ of the form,

$$\begin{aligned}\mathcal{H}_{\mathcal{R}} = {} & \lambda_1\hat{a}_1^\dagger\hat{b}_1 + \lambda_2\hat{a}_1\hat{b}_1^\dagger + \lambda_3\hat{a}_2^\dagger\hat{b}_2 + \lambda_4\hat{a}_2\hat{b}_2^\dagger \\ & + \lambda_5\hat{a}_1^\dagger\hat{a}_1\hat{b}_1^\dagger\hat{b}_1 + \lambda_6\hat{a}_2^\dagger\hat{a}_2\hat{b}_2^\dagger\hat{b}_2 \\ & + \lambda_7(\hat{a}_1^\dagger + \hat{a}_2^\dagger)\hat{c} + \lambda_8(\hat{a}_1 + \hat{a}_2)\hat{c}^\dagger, \end{aligned} \tag{9}$$

where the $\hat{b}_i$'s are the operators for the internal bath of each SQD, respectively (for example, coupling to the internal phonon modes of each dot), the $\hat{c}$ operators denote the bath processes that are common to both SQDs, and λ_i's are yet undetermined constants. The first four terms represent the noncollective portion of spontaneous emission and excitation, due to a possible symmetry breaking between the two particles as well as optical phonons inside each SQD. The next two terms are due to scattering and give rise to pure dephasing. We imagine this process to be dominated by acoustic phonon-electron coupling[28] within each SQD separately and thus treat it completely noncollectively. The final two terms represent the collective portion of spontaneous emission and excitation.

From Eq. (9), we make six Lindblad terms, ignoring those generated by $\hat{a}_1^\dagger$ and $\hat{a}_2^\dagger$ as they would represent bath-induced excitation and we are imagining our bath to be at a much lower temperature than needed to induce an excitation at the optical energy scale. We can now write our relaxation matrix as

$$\begin{aligned} -\Gamma = {} & \frac{1}{\tau_1}\mathcal{L}(\hat{a}_1,\hat{a}_1) + \frac{1}{\tau_2}\mathcal{L}(\hat{a}_2,\hat{a}_2) + \frac{1}{T_1}\mathcal{L}(\hat{a}_1^\dagger\hat{a}_1,\hat{a}_1^\dagger\hat{a}_1) \\ & + \frac{1}{T_2}\mathcal{L}(\hat{a}_2^\dagger\hat{a}_2,\hat{a}_2^\dagger\hat{a}_2) + \frac{1}{\tau_c}\mathcal{L}(\hat{a}_1 + \hat{a}_2,\hat{a}_1 + \hat{a}_2). \end{aligned}$$

τ_c is the collective decoherence and can be calculated with molecular QED. For two identical particles with a spontaneous decay rate $\frac{1}{\tau}$, then we find τ_c as

$$\begin{aligned} \tau_c = {} & \frac{2\tau}{3}\Bigg[1 - [\cos^2(\theta)]\frac{\sin(\zeta)}{\zeta} \\ & + [1 - 3\cos^2(\theta)]\left(\frac{\cos(\zeta)}{\zeta^2} - \frac{\sin(\zeta)}{\zeta^3}\right)\Bigg], \end{aligned}$$

with ζ and θ as before.

B. Numerical results

Solving the master equation (5) with our quantum interaction Hamiltonian, we find that the system no longer exhibits the behavior of the chaotic regime. For example, with $\mu_1 = 3.0$ e nm, $\mu_2 = \mu_1(1 + 10^{-3})$, $R_1 = R_2 = 13$ nm, and $a = 0$, the system shows a broad smooth response (see Fig. 10). While these parameter values led to the chaotic behavior in the semiclassical approach (upper left of Fig. 5), the chaotic behavior does not emerge in the quantum mechanic approach even for larger μ_1 or arbitrarily large symmetry breaking. Furthermore, this remains true even when the decoherence is treated completely noncollectively as in the last section.

Also in Fig. 10, we notice that the response in ρ_{11} and ρ_{22} (similarly ρ_{33}) is much broader than that of ρ_{44}. Additionally, whereas ρ_{11} and ρ_{44} both appear to reach a

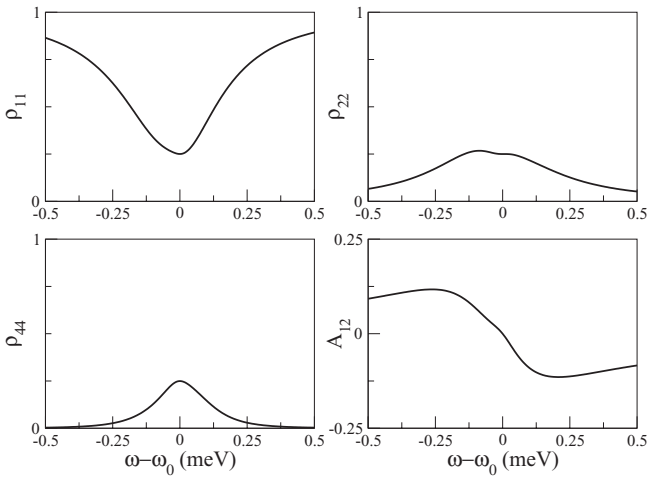

FIG. 10. Density matrix for a quantum mechanical coupling between the dots. In this approach, the chaotic regime disappears. The parameters used [$\mu_1 = 3.0$ e nm, $\mu_2 = \mu_1(1 + 10^{-3})$, $R_1 = R_2 =$ 13 nm, $\omega_0 \equiv \omega_1 = \omega_2$, and a=0] are the same used to generate the upper left plot of Fig. 5 using the semiclassical approach.

resonance value near $\omega - \omega_0 = 0$, ρ_{22} has two peaks (similarly for ρ_{33}), one above and one below the frequency $\omega = \omega_0$. The reason for this asymmetry of the density matrix elements is that when a quantum mechanical coupling is used for the interaction between the two dots, this introduces a splitting between the two singly excited states. Thus, the symmetric and antisymmetric states have different energy eigenvalues, with the symmetric state being below the bare resonance and the antisymmetric state being at a higher energy than the bare resonance. This feature of the quantum mechanical coupling gives rise to a dipole blockade, which is absent in the semiclassical model, which we examine next.

C. Dipole blockade

As the strength of the dipole-dipole coupling between the SQDs is increased (either by decreasing their separation or increasing their respective dipole moments), the symmetric (antisymmetric) eigenstate shifts to a lower (higher) energy. Thus, each of the single-exciton states is further detuned from the bare resonance. However, the doubly excited state remains located at the bare resonance. Therefore, if the system is driven at this frequency $\omega = \omega_0$, the excitation of the singly excited states would be suppressed owing to their respective detuning. This loss of population in the symmetric and antisymmetric states then results in an increase in the ground and doubly excited states in the steady-state limit. Conversely, if the system is driven near the symmetric or antisymmetric mode, then the doubly excited state, being detuned from this frequency, would be suppressed. This suppression of the doubly excited state due to the increased occupation of the single excited states is often referred to as a dipole blockade.

To expand on the idea of dipole blockade, we first consider the probability for each of the SQDs to be excited. From the density matrix, we can say that $(\rho_{22} + \rho_{44})$ is the probability that SQD1 is excited and $(\rho_{33} + \rho_{44})$ is the probability that SQD2 is excited. Thus, we expect the product of these two probabilities to be approximately equal to the probability that

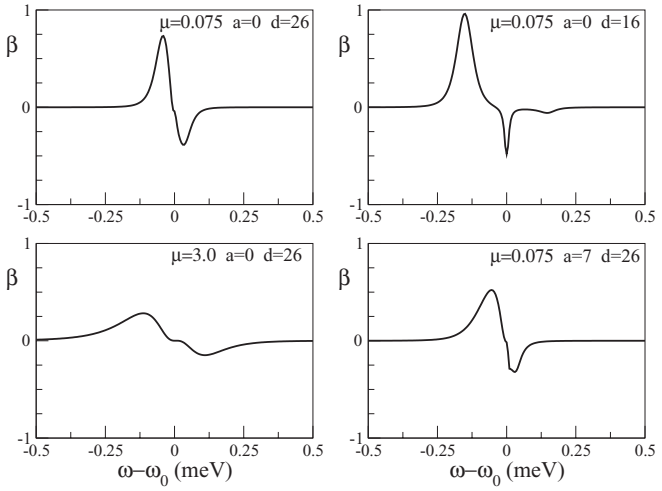

FIG. 11. Dipole blockade measure β as a function of the detuning for various values of system parameters. Blockade increases with decrease in dot-to-dot separation (increased coupling) and decreases with response broadening (increased coupling to the driving field or MNP) ($\omega_0 \equiv \omega_1 = \omega_2$).

both SQDs are excited at the same time, and therefore equal to ρ_{44}. The difference between these two probabilities can then be used as a measure of how suppressed or enhanced excitation of the doubly excited state is. To quantify the degree of dipole blockade in the system, we define the following measure β:

$$\beta \equiv 9 * [(\rho_{22} + \rho_{44})(\rho_{33} + \rho_{44}) - \rho_{44}]. \tag{10}$$

The factor of 9 in the definition of β is chosen so that with full blockade, i.e., $\rho_{44} = 0$, at saturation ($\rho_{11} = \rho_{22} = \rho_{33} = \frac{1}{3}$), $\beta = 1$. This is essentially the maximum value of β in the steady-state limit (without population inversion). Conversely, if the interaction between the dots is strong enough, then their resonances will be shifted with respect to their bare resonances. In such a case, with the driving field near the bare SQD resonance, the excitation of a single SQD, ρ_{22} and ρ_{33}, will be suppressed relative to ρ_{44} and $\beta < 0$. In our calculations, values of $\beta < -0.5$ were rare.

When we plot β for various values of the system parameters, we find that blockade increases when the SQD–SQD separation is decreased as expected (see Fig. 11). The stronger coupling between the dots increases the splitting between the two levels. For a detuning near the symmetric mode resonance, that mode is much more likely to be filled than the antisymmetric state, which is at a much higher energy, thus double excitation of the dots is suppressed. When coupling to the driving field is increased (by increasing μ) or coupling to the MNP is increased (by increasing a), the SQD response broadens, providing more overlap between the two single-exciton states and thus the dipole blockade is decreased.

D. Comparison in the weak SQD–SQD coupling regime

When there is strong SQD–SQD coupling, the semiclassical and quantum approaches produce very different results. However, when the direct coupling between the SQDs is weaker, the detuning of the symmetric and antisymmetric states is smaller. Furthermore, in the presence of an MNP, the coupling

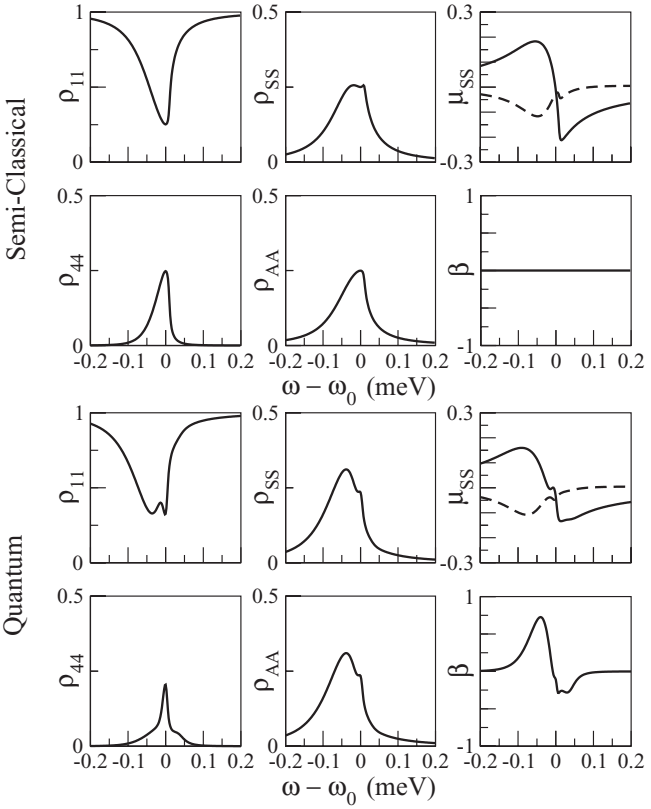

FIG. 12. Comparison between the semiclassical model (top six plots) and quantum model (bottom six plots) in the regime with weak SQD–SQD coupling ($\mu_1 = \mu_2 = 0.5$ e nm), and strong SQD–MNP coupling ($a = 7$ nm, $R_1 = R_2 = 13$ nm). Shown for each model are the diagonal density matrix elements of the symmetric/antisymmetric basis ($\rho_{11}, \rho_{SS}, \rho_{AA}, \rho_{44}$) and the blockade measure β. Also shown are the real (solid line) and imaginary (dotted line) parts of the transition dipole moment of the symmetric state $\mu_{SS} = \rho_{1S} + \rho_{S1} + \rho_{S4} + \rho_{4S}$.

mediated by the plasmons can become more significant than the direct coupling between the SQDs. It is then expected that the two approaches would be more in agreement in this regime.

When the two models are compared (top versus bottom of Fig. 12), we see similarities between the semiclassical and quantum models in the general shape of the predicted responses. However, there is significant deviation between the two models as well. In particular, the semiclassical approach does not account for the dipole blockade that occurs in the quantum model. Even with weak SQD–SQD coupling, the dipole blockade can still have a significant impact on system behavior. This leads to noted differences between the two models in the regions just above and below the SQD bare resonance, where β reaches extrema values.

In the quantum model, the differences highlighted in Fig. 12 are most notable in the slight splitting shown in ρ_{11}, very sharp peak of ρ_{44}, and the enhancement in ρ_{SS} (which we calculate as $\mu_{SS} = \rho_{1S} + \rho_{S1} + \rho_{S4} + \rho_{4S}$) that occurs just below the SQD bare resonance. These effects are due to dipole blockade. In the case of ρ_{SS}, this enhancement is just the location of the symmetric eigenstate. Interestingly, ρ_{AA} is also peaked at this same energy and appears to be identical to ρ_{SS}. However, the reason that $\rho_{SS} = \rho_{AA}$ in the steady-state limit is simply due to

mixing between the symmetric and antisymmetric modes from the interaction with the bath. Note that there is no corresponding peak in the response of the system above resonance where the antisymmetric eigenstate is located. This is because the antisymmetric state is not coupled to the driving field. When the system is driven near this frequency, the only single-exciton state coupled to the driving field is the symmetric mode which is far detuned in this case. Thus, the double-exciton state, being closer in resonance with the driving field, is enhanced compared to ρ_{SS}. Thus, $\beta < 0$ above resonance.

V. CONCLUSIONS

We have studied the response of a hybrid nanostructure molecule consisting of two SQDs coupled to a centrally located MNP, driven by an applied electric field. We have focused on identifying and addressing the issues in modeling such a system. A semiclassical approach to model the coupling between the SQDs can lead to unstable, oscillatory, and chaotic behavior in a strong SQD–SQD coupling regime. This nonlinear behavior was shown to be due to a breaking of the identical particle symmetry. Additionally, we saw that this chaotic behavior is closely related to the type of decoherence present in the system, specifically, whether the decoherence is collective or noncollective between the two SQDs. Treating the coupling of each SQD to the bath separately (noncollectively) breaks the identical particle symmetry and allows the antisymmetric single-exciton state to couple to the other states in the system. We then modeled the system using a quantum mechanical expression for the SQD–SQD coupling, and saw that this instability in the response is absent. Whereas in the semiclassical model, a large SQD–SQD coupling leads to a chaotic response, in the quantum mechanical model, strong SQD–SQD coupling produced a large splitting between the two single-exciton states that gives rise to dipole blockade. We then compared the two models on a system with a strong plasmon-mediated interaction between the SQDs and a weak direct interaction between them. In this case, we found that while the results of the two models were similar, dipole blockade and the level splitting of the single-exciton states in the quantum model are nontrivial effects even in this Regime.

*Corresponding author: ryan.artuso@nist.gov

[1] M. L. Brongersma, J. W. Hartman, and H. A. Atwater, Phys. Rev. B **62**, R16356 (2000).
[2] A. Gonzalez-Tudela, D. Martin-Cano, E. Moreno, L. Martin-Moreno, C. Tejedor, and F. J. Garcia-Vidal, Phys. Rev. Lett. **106**, 020501 (2011).
[3] A. V. Akimov, A. Mukherjee, C. L. Yu, D. E. Chang, A. S. Zibrov, P. R. Hemmer, H. Park, and M. D. Lukin, Nature (London) **450**, 402 (2007).
[4] Y. Fedutik, V. V. Temnov, O. Schops, U. Woggon, and M. V. Artemyev, Phys. Rev. Lett. **99**, 136802 (2007).
[5] H. Mertens, J. S. Biteen, H. A. Atwater, and A. Polman, Nano Lett. **6**, 2622 (2006).
[6] A. G. Curto, G. Volpe, T. H. Taminiau, M. P. Kreuzer, R. Quidant, and N. F. van Hulst, Science **329**, 930 (2010).
[7] E. Altewischer, M. P. van Exter, and J. P. Woerdman, Nature (London) **418**, 304 (2002).
[8] S. Fasel, F. Robin, E. Moreno, D. Erni, N. Gisin, and H. Zbinden, Phys. Rev. Lett. **94**, 110501 (2005).
[9] G. Di Martino, Y. Sonnefraud, S. Kena-Cohen, M. Tame, S. K. Ozdemir, M. S. Kim, and S. A. Maier, Nano Lett. **12**, 2504 (2012).
[10] O. Mollet, S. Huant, G. Dantelle, T. Gacoin, and A. Drezet, Phys. Rev. B **86**, 045401 (2012).
[11] C. Gruber, P. Kusar, A. Hohenau, and J. R. Krenn, Appl. Phys. Lett. **100**, 231102 (2012).
[12] Wei Zhang, A. O. Govorov, and G. W. Bryant, Phys. Rev. Lett. **97**, 146804 (2006).
[13] R. D. Artuso and G. W. Bryant, Nano Lett. **8**, 2106 (2008).
[14] R. D. Artuso and G. W. Bryant, Phys. Rev. B **82**, 195419 (2010).
[15] R. D. Artuso, G. W. Bryant, A. Garcia-Etxarri, and J. Aizpurua, Phys. Rev. B **83**, 235406 (2011).
[16] Jie-Yun Yan, Wei Zhang, Suqing Duan, Xian-Geng Zhao, and A. O. Govorov, Phys. Rev. B **77**, 165301 (2008).
[17] A. Govorov, G. Bryant, W. Zhang, T. Skeini, J. Lee, N. Kotov, J. Slocik, and R. Naik, Nano Lett. **6**, 984 (2006).
[18] D. E. Gómez, A. Roberts, T. J. Davis, and K. C. Vernon, Phys. Rev. B **86**, 035411 (2012).
[19] Mu-Tian Cheng, Shao-Ding Liu, Hui-Jun Zhou, Zhong-Hua Hao, and Qu-Quan Wang, Opt. Lett. **32**, 2125 (2007).
[20] R. Esteban, T. V. Teperik, and J. J. Greffet, Phys. Rev. Lett. **104**, 026802 (2010).
[21] I. S. Maksymov, A. E. Miroshnichenko, and Y. S. Kivshar, Phys. Rev. A **86**, 011801 (2012).
[22] A. Ridolfo, O. Di Stefano, N. Fina, R. Saija, and S. Savasta, Phys. Rev. Lett. **105**, 263601 (2010).
[23] E. Waks and D. Sridharan, Phys. Rev. A **82**, 043845 (2010).
[24] D. Dzsotjan, A. S. Sørensen, and M. Fleischhauer, Phys. Rev. B **82**, 075427 (2010).
[25] E. Prodan and P. Nordlander, Chem. Phys. Lett. **349**, 153 (2001).
[26] E. Townsend and G. W. Bryant, Nano Lett. **12**, 429 (2012).
[27] P. Song, P. Nordlander, and S. Gao, J. Chem. Phys. **134**, 074701 (2011).
[28] J. Förstner, C. Weber, J. Danckwerts, and A. Knorr, Phys. Rev. Lett. **91**, 127401 (2003).
[29] L. D. Landau, E. M. Lifshitz, and L. P. Pitaevskii, *Electrodynamics of Continuous Media* (Butterworth-Heinemann, Oxford, 1984).
[30] A. Yariv, *Quantum Electronics* (Wiley, New York, 1975).
[31] R. H. Lehmberg, Phys. Rev. A **2**, 883 (1970).
[32] P. B. Johnson and R. W. Christy, Phys. Rev. B **6**, 4370 (1972).
[33] K. L. Silverman, R. P. Mirin, S. T. Cundiff, and A. G. Norman, Appl. Phys. Lett. **82**, 4552 (2003).
[34] T. H. Stievater, Xiaoqin Li, D. G. Steel, D. Gammon, D. S. Katzer, D. Park, C. Piermarocchi, and L. J. Sham, Phys. Rev. Lett. **87**, 133603 (2001).